

Dual-recycled cavity-enhanced Michelson interferometer for gravitational-wave detection

Guido Müller, Tom Delker, David B. Tanner, and David Reitze

The baseline design for an Advanced Laser Interferometer Gravitational-Wave Observatory (Advanced LIGO) is a dual-recycled Michelson interferometer with cavities in each of the Michelson interferometer arms. We describe one possible length-sensing and control scheme for such a dual-recycled, cavity-enhanced Michelson interferometer. We discuss the principles of this scheme and derive the first-order sensing signals. We also present a successful experimental verification of our length-sensing system using a prototype tabletop interferometer. Our results demonstrate the robustness of the scheme against deviations from the idealized design. We also identify potential weaknesses and discuss possible improvements. These results as well as other benchtop experiments that we present form the basis for a sensing and control scheme for Advanced LIGO. © 2003 Optical Society of America

OCIS codes: 120.3180, 120.5050, 120.2230, 350.1270.

1. Introduction

Interferometric gravitational-wave observatories aim to detect gravitational waves for the first time. When successful, these observatories will not only confirm an essential part of Einstein's general relativity theory, they will also open a completely new window to the universe. Gravitational waves are generated by large accelerated masses. Most of the potential sources, supernovas, black hole binaries, and neutron star mergers, are some of the most violent processes in the universe. A large fraction of their energy is emitted by gravitational radiation.

The first generation of large-scale interferometric gravitational-wave detectors is now being built. In the United States, the three Laser Interferometer Gravitational Wave Observatory (LIGO)¹ detectors are composed of two 4-km-long and one 2-km-long power-recycled cavity-enhanced Michelson interferometers (MIs) located in Livingston, Louisiana, and in Hanford, Washington. Near Hanover, Germany, the German-British GEO² collaboration is building a 600-m dual-recycled MI. The Japanese TAMA³ collaboration is constructing a 300-m LIGO-

type detector. The 3-km French-Italian VIRGO⁴ detector is being built in the vicinity of Pisa, Italy. All these detectors are expected to reach a displacement sensitivity of the order of 10^{-19} m/ $\sqrt{\text{Hz}}$ around a few hundred hertz. Although this is already an astonishing sensitivity, theoretical predictions of gravitational-wave emissions for supernovas and other sources indicate that only the strongest events will produce enough gravitational strain to be detectable. Along with the construction and commissioning of the first generation of large-scale detectors, planning and research for a second generation of more sensitive detectors is under way. The key changes for this upgrade in LIGO⁵ are a substantial increase in the laser power from around 10 to 150 W, improved seismic isolation, and a change in the interferometer topology called signal recycling (SR) or, alternatively, resonant sideband extraction. This last improvement adds an additional mirror to the interferometer and builds up the signal sideband in the interferometer before releasing it to the photodetector. This additional mirror adds an additional degree of freedom to the interferometer and the optical configuration and makes it necessary to implement a new length-sensing scheme.

In this paper we describe the principals and the experimental realization of a length-sensing and control scheme for a dual-recycled cavity-enhanced MI. It is part of a series of four papers, all published in this issue. Strain *et al.*⁶ introduce the reader to the problems of length sensing and control in laser interferometric gravitational-wave detectors, discuss

The authors are with the Department of Physics, B100 New Physics Building, University of Florida, Gainesville, Florida 32611-8440. G. Müller's e-mail address is mueller@phys.ufl.edu.

Received 5 July 2002; revised manuscript received 18 October 2002.

0003-6935/03/071257-12\$15.00/0

© 2003 Optical Society of America

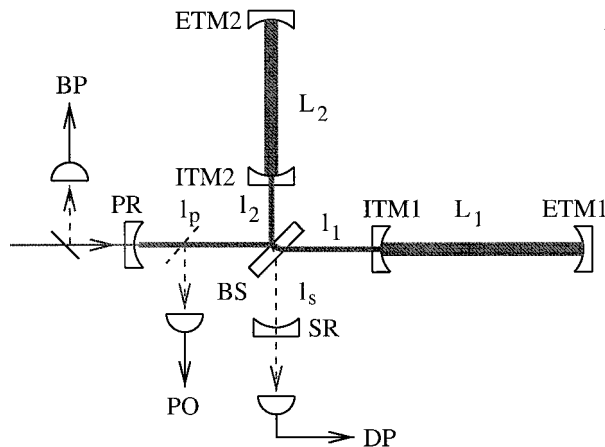


Table 1. Five Relevant Longitudinal Degrees of Freedom in an Advanced LIGO^a

Description	Symbol	Physical Distance
Differential arm cavity	Φ_-	$2k (L_1 - L_2)$
Common arm cavity	Φ_+	$2k (L_1 + L_2)$
Differential Michelson	ϕ_-	$k (l_1 - l_2)$
PR cavity	ϕ_+	$k (2l_p + l_1 + l_2)$
SR cavity	ϕ_s	$k (2l_s + l_1 + l_2)$

^aIt is convenient to describe the two arm cavities by use of their average or common length and their length difference or differential length instead of the individual lengths. The wave number is $k = 2\pi/\lambda$.

Fig. 1. Advanced LIGO consists of two arm cavities formed between the input test mass ITM1(2) and the end test mass ETM1(2) of length L_1 and L_2 . The distances of the arm cavities from the beam splitter are l_1 and l_2 . These arm cavities in conjunction with the beam splitter (BS) form the Michelson interferometer (MI). The power-recycling mirror (PR) at a distance l_p in front of the beam splitter and the signal-recycling mirror (SR) at l_s behind the beam splitter complete the interferometer. The lengths L_i of the arm cavities are approximately 4000 m, whereas the other distances are of the order of a few meters up to probably 20 m. These distances depend on the final length-sensing scheme and have to match the used modulation frequencies. We use three different detection ports for length sensing and control: the dark port (DP), the bright port (BP), and the pickoff (PO).

some common features of all three sensing schemes, and put the results in perspective for the Advanced LIGO detector. In this paper we describe different realizations of length-sensing and control schemes (see also Refs. 7 and 8). In Section 2 of this paper we focus on the restrictions and on the general ideas that influenced our sensing scheme. In Section 3 we describe the experimental layout and the realization, and in Section 4 we describe the experimental results. In Section 5 we discuss briefly the specific results and how they influenced the baseline scheme for the Advanced LIGO detector. A longer discussion of all the results and their impact on the Advanced LIGO research can be found in the introductory paper.⁶

2. General Considerations

The five different longitudinal degrees of freedom in an advanced gravitational-wave detector are the differential and common arm cavity lengths, the differential MI length, the length of the power-recycling (PR) cavity, and the length of the SR cavity (see Fig. 1). The exact definitions of these degrees of freedom can be found in Table 1 and in Strain *et al.*⁶ Both arm cavity degrees of freedom will be sensed by measurement of the phase change of the main frequency component, the carrier, with respect to some local oscillators that are not resonant in the cavities. This can either be done with phase modulation techniques (sidebands) or heterodyne interferometric techniques, both discussed in Strain *et al.*⁶ in detail.

In addition to providing us with the local oscillator to detect the phase shifts caused by detuned cavities, the additional frequency components also have to sense the three auxiliary degrees of freedom, the recirculating cavities, and the differential MI degree of freedom.

There are a few restrictions on the local oscillators. These restrictions are not fundamental in nature; instead, they are based on practical or technological considerations. First, in a large-scale interferometer, all frequency components have to be a multiple of the free spectral range of the spatial mode cleaner. This spatial mode cleaner is a suspended triangular cavity with a free spectral range of a few megahertz.⁹ It is held on resonance with the fundamental spatial mode of the carrier and needs to transmit also all the other frequency components in the fundamental spatial mode. Second, we require that only serial phase modulators be used. This method is the easiest way to generate additional frequency components in a real detector. Other forms usually require an additional Mach-Zehnder interferometer in front of the main interferometer.^{7,8} Finally, the radio frequencies should not exceed 200 MHz. Obtaining shot-noise-limited photodetectors capable of handling high powers in this frequency range is nontrivial.¹⁰

The operating point for an advanced interferometric gravitational-wave detector is such that the carrier has to be resonant in both arm cavities, resonant in the PR cavity, and detuned by the right amount in the SR cavity.⁶ The interference at the beam splitter has to be such that the carrier is reflected back toward the PR mirror. This arrangement is called the dark fringe of the MI. This tuning has the following effect on the carrier: the common-mode cavity detuning Φ_+ and the detuning of the PR cavity ϕ_+ change the carrier in the pickoff and the reflected port but not in the dark port. In these common ports the transfer functions [approximations (37) and (41) in Strain *et al.*⁶] of the carrier are independent from the differential degrees of freedom Φ_- and ϕ_- and from the SR degree of freedom ϕ_s . In contrast to this, the transmitted carrier field at the dark port depends only on the two differential degrees of freedom Φ_- and ϕ_- .

The basic idea behind our sensing scheme is to use the ability of the MI to separate the common and the

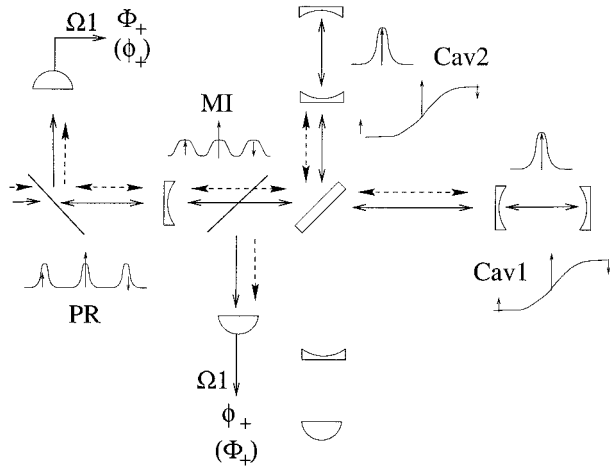


Fig. 2. First set of sidebands Ω_1 will be nonresonant in the arm cavities, dark in the MI, and slightly off resonance in the PR cavity. The reflected field will be detected to generate the error signal for the Φ_+ degree of freedom. Φ_+ will be sensed at the pickoff port. Depending on the losses and impedances of the various cavities, it could also make sense to switch the detection ports or detect both degrees of freedom at only one port as indicated by the degrees of freedom in parentheses. The inlets show the frequency of the carrier and the Ω_1 sidebands with respect to the dispersion curve of the two cavities (Cav1, Cav2), with respect to the reflectivity of the MI, and with respect to the power built up in the PR cavity.

differential degrees of freedom also in the sidebands. In addition, none of the sidebands should resonate in the arm cavities. Using the notation in Strain *et al.*,⁶ we can approximate the reflectivity of the arm cavities for all the sidebands by

$$r_{\text{cav}1(2)}(ck_{\pm i}) \approx 1 - a_{1(2)}, \quad (1)$$

where $k_{\pm i}$ is the wave number of sideband $\pm i$ ($ck_{\pm i} = \omega \pm \Omega_i$, $i = 1, 2$) and $a_{1(2)}$ is the loss in arm 1(2) in the MI. Residual small phase shifts at each arm cavity can be included in an effective overall distance between the beam splitter and the appropriate arm cavity.

A. Common Degrees of Freedom

The first set of sidebands Ω_1 is used to separate the common degrees of freedom. The sideband frequency and the asymmetry of the arm lengths in the MI are chosen so that the transmission of this pair of sidebands to the dark port is at a minimum (see Fig. 2). These sidebands should also be resonant or close to resonant in the PR cavity. The detection ports for these degrees of freedom are the pickoff and the reflected ports.

The transfer functions to the reflected and pickoff ports in first order in ϕ_+ are of the following form:

$$T(k_{\pm 1}) = T(k_{\pm 1}, \Theta) \exp(\pm i\Gamma) - i\phi_+ t(k_{\pm 1}, \Theta) \exp(\pm i\beta) \exp(\pm i\Gamma), \quad (2)$$

where, for the reflected port,

$$T(k_{\pm 1}, \Theta) \exp(\pm i\Gamma) = \frac{r_p - \exp(\pm i\Theta)(1 - \bar{a})}{1 - r_p(1 - \bar{a}) \exp(\pm i\Theta)}, \quad (3)$$

$$t(k_{\pm 1}, \Theta) \exp[\pm i(\Gamma + \beta)] = \frac{-(1 - \bar{a}) \exp(\pm i\Theta) T_p}{[1 - (1 - \bar{a}) r_p \exp(\pm i\Theta)]^2}, \quad (4)$$

and for the pickoff port,

$$T(k_{\pm 1}, \Theta) \exp(\pm i\Gamma) = \frac{t_p}{1 - r_p(1 - \bar{a}) \exp(\pm i\Theta)}, \quad (5)$$

$$t(k_{\pm 1}, \Theta) \exp[\pm i(\Gamma + \beta)] = \frac{t_p r_p (1 - \bar{a}) \exp(\pm i\Theta)}{[1 - r_p(1 - \bar{a}) \exp(\pm i\Theta)]^2}. \quad (6)$$

Here $T(k_{\pm 1}, \Theta)$ and $t(k_{\pm 1}, \Theta)$ are real, Θ is the detuning of the sideband from the PR resonance, $\pm \Gamma_r$ is the phase shift of the upper (lower) sideband of the interferometer at the working point, and β is the phase difference between the two terms (see below). The first term in Eq. (2) describes the amplitude and phase shift of the sideband at that tuning whereas the second term gives the change proportional to ϕ_+ (see Strain *et al.*⁶ for notation).

The phase shifts Γ can be compensated when we change the demodulation phase α to $\alpha + \Gamma$. The demodulated signals in both cases and both quadratures are of the following form:

$$Q = \frac{E_0^2 m}{2} [T(k_c) t(k_{\pm 1}, \Theta) \sin(\beta) \phi_+], \quad (7)$$

$$I = \frac{E_0^2 m}{2} [t(k_c) T(k_{\pm 1}, \Theta) (T_I \phi_+ + 4\Phi_+) - T(k_c) t(k_{\pm 1}, \Theta) \cos(\beta) \phi_+], \quad (8)$$

where $T(k_c)$ and $t(k_c)$ are the equivalent parts of the carrier transfer functions.⁶ The in-phase signals I in both ports can be used to generate a locking signal for Φ_+ . The quadrature signals Q can be used to generate a signal for ϕ_+ that is independent of all other degrees of freedom. The amplitude of this signal depends on the phase difference β between $T(k_{\pm 1}, \Theta)$ and $t(k_{\pm 1}, \Theta)$. It determines how far we are able to decouple ϕ_+ from Φ_+ . In the reflected port this phase difference is determined by the losses inside the interferometer:

$$\tan \beta_r \approx \frac{2\bar{a} \sin \Theta}{1 + R_p - 2r_p \cos \Theta}. \quad (9)$$

At the pickoff port it depends on the detuning of the sideband from the PR cavity:

$$\tan \beta_p = \frac{\sin \Theta}{r_p - \cos \Theta}. \quad (10)$$

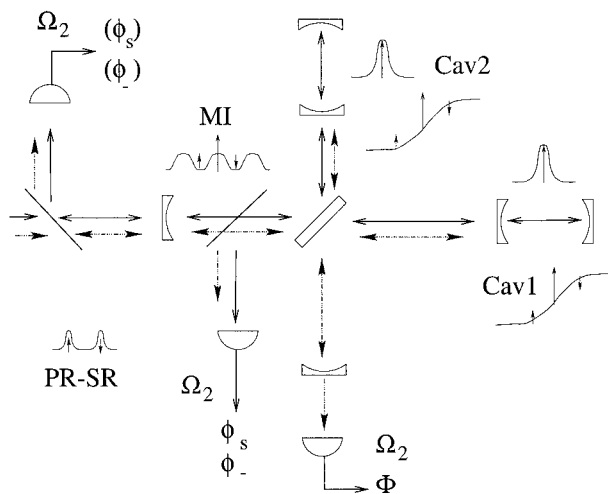


Fig. 3. Second set of sidebands Ω_2 will be nonresonant in the arm cavities, bright in the MI, and resonant in the PR-SR cavity. The pickoff field will be detected to generate the error signal for the ϕ_- degree of freedom and the ϕ_s degree of freedom. Depending on the losses and impedances of the various cavities, it could also make sense to switch to the reflected port for these signals as indicated by the degrees of freedom in parentheses. The Φ_- degree of freedom will be detected at the dark port. The inlets show the frequency of the carrier and the Ω_2 sidebands with respect to the dispersion curve of the two cavities (Cav1, Cav2), with respect to the reflectivity of the MI, and with respect to the power built up in the PR-SR cavity.

The reflected port has the disadvantage that its Q signal is sensitive to carrier losses in the interferometer. In a real gravitational-wave detector the carrier will be close to impedance matched in the interferometer and changes sign around the impedance-matching point. This effect reduces the amplitude of the Q signal with respect to the I signal, which in turn makes it more difficult to find the correct demodulation phase. The pickoff port does not have this disadvantage, and in a low-loss large-scale gravitational-wave detector it should provide us in all cases with a reasonable signal.

B. Differential Degrees of Freedom and Signal Recycling

The second pair of sidebands will provide the local oscillator at the dark port to sense Φ_- by beating with the carrier. In addition they must sense the position of the SR mirror (ϕ_s) and the status of the short MI (ϕ_-). In contrast to the carrier and the first set of sidebands, this pair will be bright in the MI (see Fig. 3). In this configuration, the sidebands can build up in the cavity that is formed between the two recycling mirrors (PR-SR cavity). The MI acts as a simple turning mirror. The sideband is resonant in the PR-SR cavity if

$$k_{\pm 2}(2l_s + 2l_p + 2\bar{l}) = 2N\pi. \quad (11)$$

This resonance condition can be divided into two different phase factors that describe the two recycling

cavities:

$$k_{\pm 2}(2l_s + 2l_p + 2\bar{l}) = \frac{k_{\pm 2}(2l_s + \bar{l})}{\pm \Theta_s} + \frac{k_{\pm 2}(2l_p + \bar{l})}{\pm \Theta_+}. \quad (12)$$

These phases are not arbitrary and can be fixed only in the design of the full interferometer. However, to fulfill the resonance condition, we require

$$\exp(-i\Theta_s) = \exp(i\Theta_+). \quad (13)$$

The resonance condition of the PR-SR cavity established in Eq. (11) will depend in first order on two of our five degrees of freedom, ϕ_s and ϕ_+ :

$$\exp[-ik_{\pm 2}(2l_s + 2l_p + \bar{l})] \approx 1 - i(\phi_+ + \phi_s). \quad (14)$$

The transfer functions for the reflected and pickoff port in first order in ϕ_+ , ϕ_s , and ϕ_- then have the following form:

$$T(k_{\pm 2}) = T^0(k_{\pm 2}) + i(\phi_+ + \phi_s)t_+^0(k_{\pm 2}) \pm (i\Delta a + \phi_-)t_-^0(k_{\pm 2}). \quad (15)$$

The abbreviations for the reflected field are

$$T^0(k_{\pm 2}) = \frac{r_p - \tilde{r}_s}{1 - r_p \tilde{r}_s}, \quad t_+^0(k_{\pm 2}) = \frac{-T_p \tilde{r}_s}{(1 - r_p \tilde{r}_s)^2}, \quad (16)$$

$$t_-^0(k_{\pm 2}) = \frac{T_p[\cos \Theta_+(1 - r_s \tilde{r}_s) \mp i \sin \Theta_+(1 + r_s \tilde{r}_s)]}{(1 - r_p \tilde{r}_s)^2}, \quad (17)$$

and for the pickoff field,

$$T^0(k_{\pm 2}) = \frac{t_p}{1 - r_p \tilde{r}_s}, \quad t_+^0(k_{\pm 2}) = \frac{t_p r_p \tilde{r}_s}{(1 - r_p \tilde{r}_s)^2}, \quad (18)$$

$$t_-^0(k_{\pm 2}) = \frac{-t_p r_p [\cos \Theta_+(1 - r_s \tilde{r}_s) \mp i \sin \Theta_+(1 + r_s \tilde{r}_s)]}{(1 - r_p \tilde{r}_s)^2}. \quad (19)$$

In the last step we included the average losses \bar{a} in the MI⁶ in \tilde{r}_s :

$$\tilde{r}_s \equiv r_s(1 - 2\bar{a}). \quad (20)$$

The demodulated signals at the bright and pickoff port are

$$Q = 2T^0(k_c)\mathcal{R}[t_-^0(k_{\pm 2})]\phi_-, \quad (21)$$

$$I = t^0(k_c)T^0(k_{\pm 2})(T_I\phi_+ + 2\Phi_+) - 2T^0(k_c)t_+^0(k_{\pm 2}) \times (\phi_+ + \phi_s) + 2T^0(k_c)\mathcal{F}[t_-^0(k_{\pm 2})]\phi_-. \quad (22)$$

At a phase $\Theta_+ = N\pi$ only the quadrature signal Q depends on ϕ_- , and the in-phase signal I depends only on the common degrees of freedom Φ_+ , ϕ_+ , and ϕ_s . The first two degrees of freedom should be already locked by the common-mode servos (see above). Similar to the Q signal in the reflected port at Ω_1 , the Q signal in the reflected port at Ω_2 scales with the

on-resonance reflectivity of the carrier and the losses in the interferometer.

The transfer function to the transmitted port can be written in a similar form:

$$T(k_{\pm 2}) = T^0(k_{\pm 2}) + i(\phi_+ + \phi_s)t_{\pm}^0(k_{\pm 2}) - (i\Delta a + \phi_-)t_{\pm}^0(k_{\pm 2}), \quad (23)$$

$$T^0(k_{\pm 2}) = \mp \frac{i\tilde{t}_s t_p}{1 - r_p \tilde{r}_s}, \quad t_{\pm}^0(k_{\pm 2}) = \mp \frac{\tilde{t}_s t_p r_p \tilde{r}_s}{(1 - r_p \tilde{r}_s)^2}, \quad (24)$$

$$t_{-}^0(k_{\pm 2}) = i\tilde{t}_s t_p \frac{(r_s - r_p)\cos \Theta_+ + i(r_s + r_p)\sin \Theta_+}{(1 - r_p \tilde{r}_s)^2}. \quad (25)$$

The important quadrature component in the demodulated signal at the dark port is

$$I = 2T^0(k_{\pm 2})t^0(k_c)(T_I\phi_- + 2\Phi_-). \quad (26)$$

This signal is the readout of the gravitational-wave detector and also the last error signal we need to plan the overall sensing scheme.

For the benchtop experiment we note one final point: The basic sensing scheme described above must be slightly modified. The interference conditions for the two pairs of sidebands in an ideal MI (Ω_1 dark, Ω_2 bright) naturally require that the two frequencies are multiples of each other. In addition, we do not want to use modulation frequencies below 30 MHz. Otherwise the lengths of the different recycling cavities would be longer than 10 m and would require additional folding of the beams, subsequently higher losses, and additional noise. A MI in which the 30-MHz sidebands are bright will be dark for 60-MHz sidebands and multiples of 60 MHz. As we have access to components that can be tuned to 60 MHz, we decided to use this frequency. But an exact tuning of the two frequencies to these values is not recommended because the second-order sidebands generated in the 30-MHz modulator will interfere with the 60-MHz sidebands of the second modulator. On the other hand, we still require that one set of sidebands be as bright as possible and one set be as dark as possible in the MI. One way to circumvent these contradicting requirements is to allow the sidebands to undergo phase shifts at the arm cavities. Thus far we assumed that the arm cavities will not alter the phase of the sidebands at all. This statement is true only if the sidebands are exactly anti-resonant. Otherwise, the sidebands will always encounter a small phase shift upon reflection at the arm cavities. The phase shift will be different in the two arms unless the arm cavities are exactly the same. This difference in the phase shifts can be used to alter the modulation frequencies slightly. Other than this, the sensing scheme is similar to the one described above.

Table 2. Measured Reflectivities of the Different Mirrors in the Interferometer^a

Parameter	Reflectivity (%)
PR	82.4
In-line input (ITM1)	90.9
In-line end (ETM1)	99.84
Perpendicular input (ITM2)	90.7
Perpendicular end (ETM2)	99.87
SR (double pass)	86.1
Beam splitter	50

^aNote that the reflectivity of the SR mirror is the square of the physical reflectivity of the turning mirror to include the fact that it reflects the field twice (see Fig. 5).

3. Experiment

A. Design

For our experiment the lengths of the two cavities were chosen to be 0.15 and 0.3 m, respectively. The reflectivities of all the mirrors were measured, and the results are shown in Table 2. The phase shifts at the two arm cavities for each sideband were then calculated. The next step was to optimize the difference of the arm lengths ($l_1 - l_2$) in the MI to maximize its reflectivity for the $\Omega_1 = 2\pi f_1$ sidebands:

$$\frac{2\pi f_1}{c}(l_1 - l_2) - \varphi_1(f_1) + \varphi_2(f_1) \approx \pi, \quad (27)$$

where $\varphi_{1(2)}(f_1)$ is the phase shift of the $f_1 = 60$ -MHz sideband at arm cavity 1(2). The optimum length difference is 2.545 m. The frequency f_2 at which the reflectivity of the MI is at a minimum has changed to 31.8 MHz because the phase difference $[\varphi_1(f) - \varphi_2(f)]$ for f_2 is different from that for f_1 .

The length of the PR cavity was not chosen to be resonant with the f_1 sidebands, but optimized to decouple the ϕ_- and ϕ_s degrees of freedom [see Eq. (22) and accompanying text]:

$$\Theta_+ = \frac{2\pi f_2}{c}(2l_p + \bar{l}) - \frac{\varphi_1(f_2) + \varphi_2(f_2)}{2} \approx \pi. \quad (28)$$

We then checked to see if the f_1 sidebands were still close to resonant in the PR cavity. This set the distance between the PR mirror and the beam splitter. The last length needed was the distance between the SR mirror and the beam splitter. This length was

Table 3. Modulation Frequencies and Distances of the Final Design of the Interferometer

Parameter	Value
f_1	60 MHz
f_2	31.8 MHz
L_1	0.15 m
L_2	0.3 m
l_1	2.788 m
l_2	0.243 m
l_p	1.12 m
l_s	3.478 m

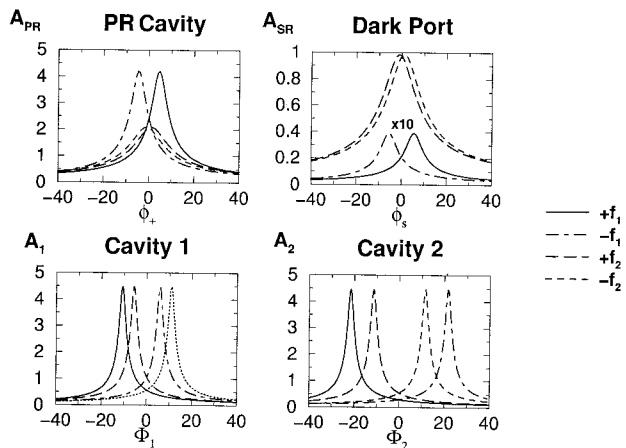


Fig. 4. Modeled amplitudes of the sidebands at different locations versus different tunings in our benchtop interferometer. The upper-left graph shows the amplitudes in the PR cavity versus the tuning of the PR cavity; the upper-right graph shows the amplitudes behind the SR mirror versus the tuning of the SR cavity. The 60-MHz sidebands are amplified by a factor of 10. The lower graphs show the amplitudes in the two arm cavities versus the arm cavity tunings.

defined by the condition that the f_2 sidebands had to be resonant in the PR-SR cavity. The final design values are shown in Table 3.

The calculated amplitudes¹¹ versus different detunings at different locations in the interferometer are shown in Fig. 4. The upper-left graph shows that the 60-MHz sidebands in the PR cavity were detuned by roughly half of the linewidth to generate

orthogonal signals for the two common degrees of freedom ϕ_+ and Φ_+ [see Eqs. (7) and (8)]. These sidebands were also close to resonance in the SR cavity as can be seen in the upper-right graph. Both upper curves show also that the 31.8-MHz sidebands were resonant in the PR-SR cavity. The lower graphs show the detuning of the sidebands with respect to the arm cavities.

B. Experimental Setup

Figure 5 shows the actual table layout. The optical table is a custom-made 20 ft. by 4 ft. (6 m by 1 m) table. The longer length allowed the excessive lengths to be incorporated in the design without the added complexity of folding the arms of the MI.

A Lightwave Electronics Model 126-1064-700 Nd:YAG nonplanar ring oscillator laser with a nominal wavelength of 1.064 μm and 700-mW maximum output power is used in this experiment. The beam is first isolated and then modulated by two electro-optic modulators (New Focus Model 4003). The beam is then mode matched so that it enters the interferometer with the proper Gaussian mode. A half-wave plate and a polarizer directly before the interferometer act as an intensity adjustment. Ideally, the reflected beam from the interferometer is separated from the incoming beam by a Faraday isolator. In this experiment we have enough extra laser power to simply use a 50/50 cubic beam splitter to pick off half of the reflected light.

The light enters the interferometer through a 1-in. (2.54-cm) PR mirror. The first optic encountered after the PR mirror (M_{PR}) is a thin glass plate (a cov-

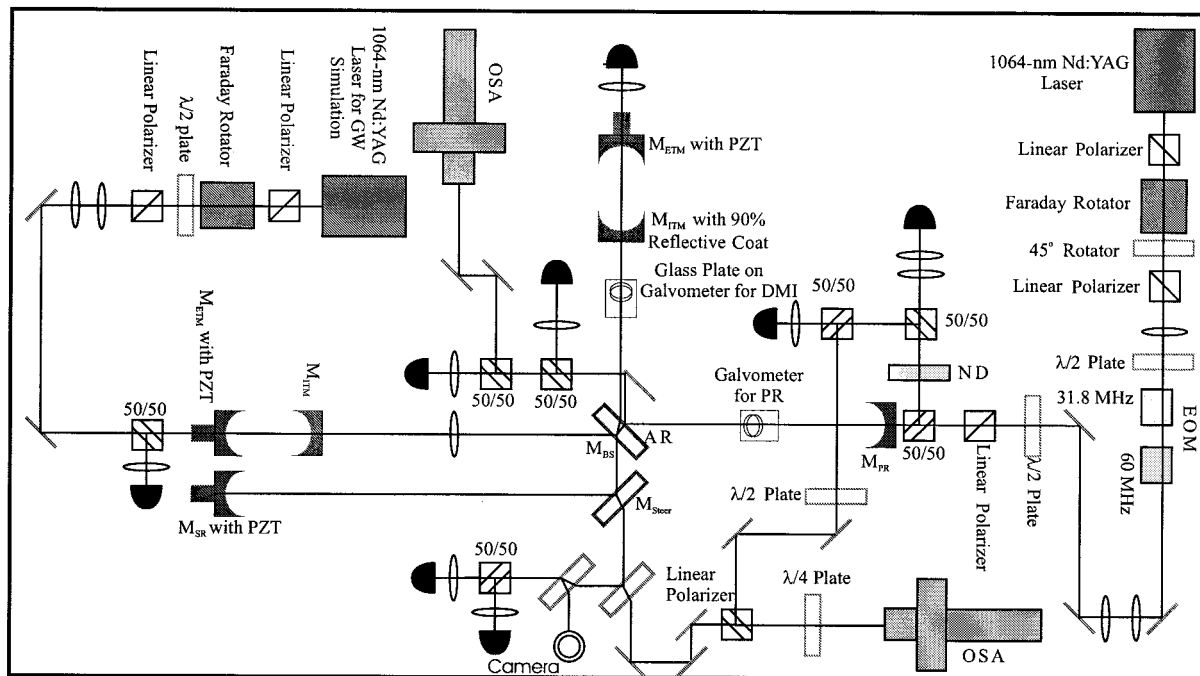


Fig. 5. Layout of the benchtop experiment at the University of Florida. The details are described in the text. GW, gravitational wave; BS, beam splitter; EOM, electro-optic modulator; AR, antireflection; ND, neutral-density filter; DMI, differential MI; ETM, end test mass; ITM, input test mass.

erslip for a microscope slide) glued to a galvanometer and set at Brewster's angle. The galvanometer is a GSI Lumonics Model G-102. This actuator controls the PR degree of freedom.

The next optic encountered is the 2-in. (5-cm-) diameter beam splitter (M_{BS}). The antireflection-coated side of the beam splitter faces the PR mirror. This provides a convenient beam for the pickoff port. The beam splitter requires a 2-in. clear aperture for beam clearance.

The perpendicular arm again has a galvanometer in it for control of the differential MI degree of freedom. A lens with a focal length of 813.4 mm is placed 1.08 m in front of the in-line arm cavity. To perfectly match the mode, two free parameters are needed. We used the focal length and the distance to the cavity. Modeling showed that this solution allows 99% of the Gaussian TEM_{00} mode to be matched into the in-line arm cavity mode.

The arm cavities themselves are fixed-spacer cavities with stainless steel used as the spacer material. The laser and arm cavities are stable without feedback. If a single cavity is tuned to resonance by a dc offset and is allowed to drift, it takes several seconds to move out of resonance. The mirrors are glued to an end cap, which is secured to the spacer with three screws. A Viton O ring is sandwiched between the end cap and the bulk of the spacer. This O ring allows independent alignment of the mirrors. The entire spacer is mounted in a large 2-in. mirror mount. The end mirrors of the arm cavities and the SR cavity end mirror (M_{SR}) are controlled by piezoelectric translator (PZT) tubes. The tubes allow the monitoring of light transmitted through the end mirrors. The mirrors are glued to the PZTs with epoxy.

The SR arm is folded by a partly transmissive steering mirror (M_{Steer}). The dark port signal is measured behind this steering mirror instead of behind M_{SR} . This design has the advantage that the dark port signal is accessible even with a blocked SR cavity.

The photodetectors used for length sensing are resonant photodetectors built in-house. There are two outputs. The dc output is simply a buffered current-to-voltage convertor. The ac output is tuned to the appropriate frequency, either 31.8 or 60 MHz. The diodes themselves are EG&G FND-100. Each of the reflected, antisymmetric, and pickoff ports has a 31.8- and 60-MHz photodetector.

The optical spectrum analyzers (OSAs) are used to characterize the distribution of sideband power in the interferometer. This proved to be a crucial tool to assess the status of the system. By measuring the amount of power in the carrier and sidebands, we are able to determine the lock state of the interferometer. They are also used to measure the losses in the system. There are two OSAs used to measure three ports. One OSA is positioned to measure the spectrum at the pickoff. The second OSA is set up to measure the dark port and the reflected port. By blocking the beam from the one port, the other port can be measured. A quarter-wave plate and a linear

polarizer are used to isolate this OSA. The other OSA is slightly misaligned for isolation.

C. Characterization of the System

1. Arm cavities

To understand the operation of the entire interferometer, we progressively characterized its subsystems. The first subsystems characterized were the arm cavities. A measurement of the on-resonance reflectivity and the finesse revealed the reflectivities of each mirror (see Table 2). The losses of the in-line arm cavity in reflection are 6.5%. The perpendicular cavity has losses of 5%. These losses tend to increase slightly in time. Occasional cleaning restores the old values. The mode matching into the perpendicular arm was measured to be approximately 97.5%. This is almost entirely limited by the astigmatism in the laser itself. The mode matching in the in-line arm is approximately 96%. During the characterization of the cavities, the PR cavity was misaligned.

2. Michelson Interferometer

The visibility of the MI was measured with locked arm cavities, a misaligned PR mirror, and a blocked SR mirror. We locked the arm cavities with the transmitted cavity fields using the leakage of the 31.8-MHz sidebands through these cavities. The transmission of the scanned MI revealed a visibility of 92%. The contrast defect is caused by slightly different transversal modes in each arm, differential losses in the cavities, and a general mode mismatch between the input field and the average interferometer mode caused by the astigmatism of the laser field.

3. LIGO I Configuration

One of the most important aspects in the design is the transmissivity of the MI for the two sets of sidebands. This was measured with the OSAs. First the SR arm was blocked and the interferometer was locked in a PR configuration with a sensing scheme similar to the one that was later used for the dual-recycled configuration. The 31.8-MHz in-phase signal at the dark port was used to lock Φ_- , the 31.8-MHz quadrature signal at the pickoff port sensed ϕ_- , the reflected in-phase signal at 60 MHz sensed Φ_+ , and the 60-MHz pickoff quadrature signal sensed ϕ_+ .

The spectra at the pickoff, at the dark port, and at the reflected port were recorded. These values were compared with the amplitudes when beam blocks were placed in front of the two arm cavities. The results are shown in Table 4. Note that the signals are not normalized and that only the values taken at the same port can be compared with the gain relative intensity information.

The first row (blocked reflection port) was used to determine the intensity in the different frequency components or the modulation indices. Each of the Ω_1 sidebands carries approximately 5.4% of the total intensity (modulation index $m = 0.47$). Each of the Ω_2 sidebands has approximately 2.4% ($m = 0.31$).

Table 4. Peak Voltage of the Different Frequency Components as Measured by the OSAs at the Different Detection Ports in the LIGO I Configuration^a

Detection Port (mV)	Carrier	$\pm\Omega_1 =$ 60 MHz	$\pm\Omega_2 =$ 31.8 MHz
Blocked reflection	4340 ± 10	278 ± 10	127 ± 5
Reflection	793 ± 100	142 ± 12	119 ± 5
Dark	19.5 ± 5	1.35 ± 0.3	3.69 ± 0.2
Pickoff	2590 ± 100	118 ± 10	1.48 ± 0.1
Blocked pickoff	49.7 ± 3	3.13 ± 0.2	1.48 ± 0.1

^aThe intensities in row 1 and 5 were measured with beam blocks in front of the arm cavities.

The input field is a linear combination of spatial interferometer eigenmodes. The intensities in the reflected and pickoff ports for the blocked arm cavities are

$$P_R(\text{blocked}) = R_p(P_0 + P_M),$$

$$P_P(\text{blocked}) = ST_p(P_0 + P_M), \quad (29)$$

where R_p and T_p are the reflectivity and transmissivity of the PR mirror and S is an as yet unknown scaling factor between the two signals. P_0 and P_M are the intensities in the fundamental and higher-order spatial modes of the interferometer. Feedback loops keep the fundamental spatial mode of the carrier resonant in all cavities and dark in the MI. The intensities in the locked case are

$$P_R(\text{locked}) \approx \left(\frac{r_p - r_{\text{MI}}}{1 - r_p r_{\text{MI}}} \right)^2 P_0 + P_M, \quad (30)$$

$$P_P(\text{locked}) \approx \frac{ST_p}{(1 - r_p r_{\text{MI}})^2} P_0. \quad (31)$$

In approximation (30) we assume that all the mismatched light is reflected at the PR cavity. This value is somewhere between unity and the reflectivity of the PR mirror. The following results do not change significantly when we change the reflectivity from unity to R_p . In approximation (31) we assume that the power inside the PR cavity in the nonresonant higher-order modes is much smaller than the power in the resonant fundamental mode. These last four equations [Eqs. (29)–(31)] can be solved for the four unknowns S , r_{MI} , P_0 , and P_M :

$$S = 5.4 \times 10^{-2}, \quad (32)$$

$$R_{\text{MI}} = r_{\text{MI}}^2 = 0.90 \pm 0.02, \quad (33)$$

$$\frac{P_M}{P_0} = \frac{242 \text{ mV} \pm 200 \text{ mV}}{5025 \text{ mV} \pm 200 \text{ mV}} = 4.8\% \pm 4.7\%. \quad (34)$$

The $\sim 90\%$ reflectivity of the MI for the carrier includes all losses in the interferometer. The gain of the carrier in the PR cavity is 9.6. The amount of mismatched light in the input beam is somewhere between 4% and 9.5%. The minus sign in the above error bar [Eq. (34)] can nearly be excluded because of

the measured mode mismatch into the simple arm cavities.

The sidebands are in the same spatial mode as the carrier, and all higher-order spatial modes are assumed to be completely reflected at the PR mirror. The gain inside the PR cavity for the slightly detuned Ω_1 sidebands is around 7.2 ± 0.2 . The accuracy is limited by the uncertainty in the mode matching. The reflectivity of the sidebands is of the order of $37 \pm 2\%$. These two values can be used to calculate the reflectivity of the cavity-enhanced MI for the Ω_1 sidebands and their detuning from the PR cavity resonance. The reflectivity is approximately $91 \pm 2\%$ with a detuning of the order of 5° or 850 ± 50 kHz.

There are no changes in the intensities of the Ω_2 sidebands between a blocked and unblocked interferometer. This indicates that the MI is bright for this sideband. Nevertheless, these intensities were used as a calibration for the various ports, which in turn were used to calculate the transmissivity of the MI for the carrier and the sidebands. We assumed that the transmission of the MI for the Ω_2 sidebands is unity. This approach gives an upper limit for the transmission of the carrier of approximately 0.3% and of the Ω_1 sidebands of approximately 0.46%. The transmission of the carrier in the nonrecycled MI is 8%, indicating that the mode mismatch between the interferometer and the laser field is 8–9% and that the recycling cavity blocks this light efficiently.

All these values are functions of the losses in the various optical components and of the real lock points of the different degrees of freedom. The losses change slowly in time because of drifts in the alignment and dust; we see this especially in the cavities. The lock points change because of drifts in the different offsets of the error signals caused either by changes in the amplitude modulation at the modulation frequency (radio-frequency amplitude modulation) or by changes in electronic offsets. One problem we ignored so far is that the spatial eigenmodes in the interferometer are slightly different for the different frequency components. This is caused by the imperfect mode matching between the arm cavities and the PR cavity. As a result, the mode-matching efficiency into the interferometer will be different for the different frequency components.

4. Dual-Recycled Configuration

The only differences between the power-recycled and the dual-recycled configurations are the inclusion of the SR mirror M_{SR} and the additional feedback loop for ϕ_s . The 31.8-MHz in-phase signal in the pickoff port was used as an error signal for ϕ_s . The OSA signals for the dual-recycled cavity-enhanced MI are shown in Table 5.

Seen from the reflected port the whole optical configuration looks like a two-mirror cavity in which the end mirror has a complex frequency-dependent reflectivity and transmissivity. Feedback loops held the carrier again on resonance in all cavities and dark in the MI. The reflectivity of the carrier of this com-

Table 5. Peak Voltage of the Different Frequency Components as Measured by the OSAs at the Different Detection Ports in the LIGO II Configuration

Detection Port (mV)	Carrier	$\pm\Omega_1 =$ 60 MHz	$\pm\Omega_2 =$ 31.8 MHz
Blocked reflection	4340 ± 10	278 ± 10	127 ± 5
Reflection	1240 ± 300	102 ± 20	60 ± 6
Dark	68.8 ± 20	39.6 ± 5	31.6 ± 2
Pickoff	2520 ± 100	43.2 ± 15	11.6 ± 1
Blocked pickoff	49.7 ± 3	3.13 ± 0.2	1.48 ± 0.1

plex end mirror was again calculated from the measured intensities:

$$R_{\text{end}} = 0.91 \pm 0.02,$$

$$\frac{P_M}{P_0} = \frac{606 \pm 220}{4661 \pm 220} = 13\% \pm 5\%.$$

As expected, the SR mirror does not change the reflectivity of the MI. The error bars in the mode matching are caused by the large power fluctuations in the reflected port. It is most likely that these fluctuations are caused by length changes in the common mode of the arm cavities. These changes decrease the average reflected power. The reflectivity at the working point would be the smallest measured value around 940 mV. In that case, the mode matching would be approximately 8%. On the other hand, fluctuations in the length of the OSA tend to reduce the average transmissivity. Our best estimate for the mode matching is 9%.

The gain of the Ω_1 sidebands in the interferometer measured at the pickoff port is 2.7. The reflectivity of the full interferometer for these sidebands at the operating point in its fundamental mode is around 23%. The SR mirror reduces the reflectivity of the MI to approximately 71% and increases the detuning in the PR cavity to 7°. These results do not change significantly if we assume a mode matching of only 87%. One possible explanation for this decrease in the MI reflectivity is an increase in the transmissivity of the MI for these sidebands to approximately 2.5% and a detuning of the SR mirror of 5.6°. This increased transmissivity could be caused by an additional offset in the MI feedback loop caused also by offsets in the SR degree of freedom.

The buildup of the Ω_2 sidebands in the PR-SR cavity can be calculated from the dark port and the pickoff signals. The intensity of the pickoff signal divided by the blocked pickoff signal times the mode matching yields a gain of 8.61. The ratio between the dark port signals with and without SR yield a gain of 8.56. The reflectivity of the fundamental spatial mode of the locked interferometer is around 33%. This reflectivity and the gain could be explained by a reflectivity of the signal-recycled MI of 56% and a phase shift of 7.6° for the sidebands. For the case in which the MI is bright for the Ω_2 sidebands, the reflectivity of the signal-recycled MI is equal to the square of the transmission of the MI

times the reflectivity of the SR arm. In turn, the latter is a few percent less than the square of the reflectivity of the steering mirror $(0.93)^2 = 0.86$ given the additional losses at the high-reflective SR mirror and the imperfect mode matching between the SR arm and the rest of the interferometer. The losses in the MI for the Ω_2 sidebands in transmission have to be at least similar to the losses for the Ω_1 sidebands in reflection, namely, 91%. Differences between the spatial eigenmode of the SR cavity compared with the eigenmode of the rest of the interferometer can increase these losses.

4. Results

Dual recycling manifests itself in several ways. The main feature is that the transfer function for the differential arm cavity degree of freedom has a higher gain and a smaller bandwidth compared with a power-recycled configuration. But dual recycling also changes the amplitude of the sidebands on the photodetector, which in turn changes the signal but also the shot noise. This additional gain would be useful only if the final detector were limited by technical noise such as electronic noise, which is not expected. It is also important to note that dual recycling will only increase our sensitivity toward gravitational waves in frequency regions where the detector is limited by shot noise and not by displacement noise.

The higher optical gain in the interferometer increased the strengths of the Φ_- error signal. In a closed-loop configuration, this increase can either decrease the residual error point noise or destabilize the feedback loop because of too much gain in frequency regions where the phase reserve is too small. To demonstrate this we first blocked the SR mirror, locked the interferometer in a power-recycled configuration, and unblocked the SR mirror. For larger electronic gains, the interferometer always lost lock. With reduced electronic gains, we were able to first lock the LIGO I configuration and then unblock the SR mirror without losing lock. Nonetheless, the configuration was oscillating around its working point at a high frequency. We further reduced the electronic gain until these oscillations were no longer obvious. At that point we measured the error point noise in both configurations and calibrated it with a 10-kHz injected signal (see Fig. 6).

Within the bandwidth of the feedback loops, the calibrated SR error point noise is approximately an order of magnitude smaller than the calibrated PR error point noise. This suppression of the displacement noise is due to the higher optical gain of the dual-recycled configuration compared with the power-recycled configuration. Near 2 kHz is a frequency band where the increased optical gain actually increases the differential motion of the mirrors. These servo bumps are the results from the oscillations mentioned above.

Above approximately 3 kHz the feedback loops have no influence on the error point noise, and both configurations show basically the same displacement

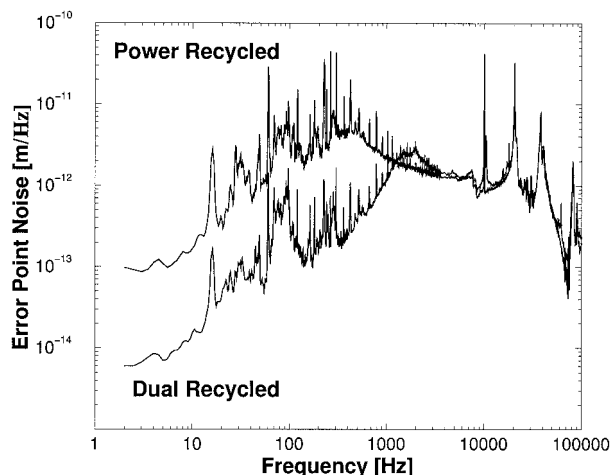


Fig. 6. Calibrated error point noise in the dual-recycled configuration in the low-frequency region is approximately an order of magnitude smaller than in the power-recycled configuration. This is caused by the larger optical gain. In the high-frequency region, the displacement noise is equal in both configurations.

noise. There were still some differences at frequencies close to the PZT resonances, where the increased optical gain increases the effective overall gain. This measurement also shows that the limiting noise source in this frequency region is displacement noise in the arms of the MI and not any electronic noise in the detection system.

The optical gain of the dual-recycled configuration can be calculated from the uncalibrated demodulated signals (Fig. 7). The peak at approximately 2 kHz is an artifact of the increased gain in the feedback loop.

The SR (amplitude) gain of 7.4 is limited by the losses in the SR cavity and the reflectivity of the SR

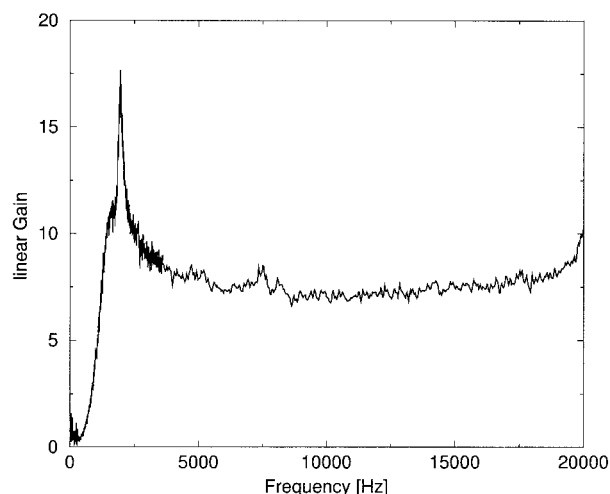


Fig. 7. Optical gain of the SR cavity. The peak at 2 kHz is an artifact of the feedback loop. The flat region above 2 kHz represents the real gain of 7.4. The increase at approximately 20 kHz is caused by a resonance at 20.5 kHz in one of the actuators.

mirror. This gain corresponds to a product of the reflectivities of the SR arm and the MI:

$$r_{\text{SR}}^2 r_{\text{MI}}^2 = \left(\frac{g_{\text{SR}} - 1}{1} \right)^2 = 0.75.$$

The reflectivity of the turning mirror in the SR arm was measured to be $r_{\text{SR}}^2 = 0.86$ (double pass), and the reflectivity of the MI for the carrier was estimated from the OSA signals to be $r_{\text{MI}}^2 = 0.9$. These numbers left approximately 2.4% of unaccounted losses, which could be caused by additional losses on the SR mirror or mode mismatches between the SR arm and the rest of the interferometer.

For the low-frequency response shown in Figs. 6 and 7, it was not necessary to inject a signal into the system. The displacement noise caused by acoustic or electronic noise in the actuators produced signals larger than the electronic noise in the photodiodes and mixers. But this low-frequency response is insufficient to show the frequency roll-off and the gain in a detuned configuration, where signals extended to few hundred kilohertz or even 1 MHz. In this case, an additional laser was injected through one of the arm cavities into the interferometer as to mimic a gravitational wave. A gravitational wave will modulate the phase of the light field in the arm cavities and add a pair of sidebands to the carrier. However, a single sideband is all that is needed to trace out the frequency response of the interferometer. The frequency of the second laser was tuned to within plus or minus a few megahertz of the main carrier. The beat of this new field with the Ω_1 sideband at the dark port was then recorded on a spectrum analyzer. The signal was taken before the mixer to ensure that it is not degraded by a misaligned demodulation phase. The measured gain was then normalized by the sideband gain (Fig. 8). A detailed description of this procedure can be found in Shaddock *et al.*⁸

The gain at low frequencies is around 16.7 dB. This confirms the low-frequency measurements. The roll-off with a 3-dB bandwidth of 335 kHz and the gain could be modeled with a SR mirror with an effective reflectivity of 78%.

As described in detail in Strain *et al.*,⁶ a resonant dual-recycled interferometer will have its peak displacement sensitivity around dc. However, sensitivity at these low frequencies is not useful to detect gravitational waves because the position of the test masses will be greatly disturbed by environmental noise sources such as seismic or thermally driven displacement noise. The interferometer becomes limited by shot noise only at or above approximately 100 Hz. Therefore SR is useful only in a gravitational-wave detector if it increases the signal in a frequency region where the detector is shot-noise limited. Detuned operation permits such an increase. There are several ways to detune the SR cavity and keep the system locked. One way is to use the beats between sidebands to control ϕ_- , ϕ_+ , and ϕ_s . This would decouple these auxiliary degrees of freedom from the arm cavity degrees of freedom Φ_+

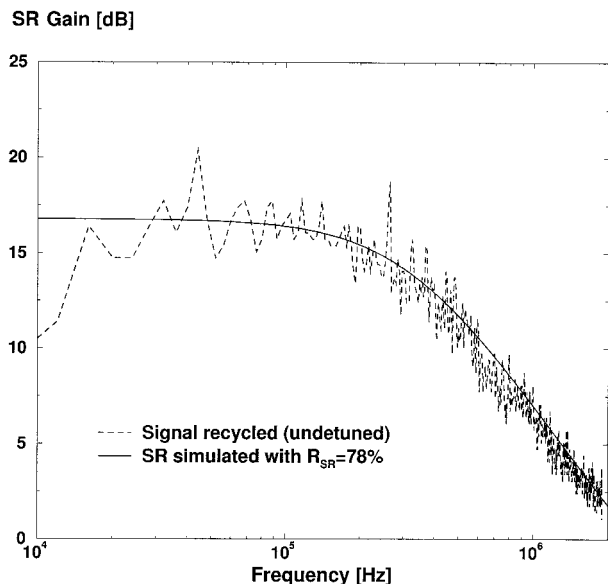


Fig. 8. SR gain is relative to a power-recycled configuration corrected for the Ω_1 sideband gain. The flat portion below 100 kHz confirms the gain measured at low frequencies. The 3-dB bandwidth is approximately 335 kHz. The simulated frequency response was calculated for a reflectivity of 78% in the SR mirror.

and Φ_- . This method was proposed and described in detail by Shaddock *et al.*⁸ We tuned the SR mirror using electronic (dc) offsets. We added an offset to the error signal for the SR cavity and detuned the SR cavity by approximately 10° (Fig. 9).

For a greater detuning (the ϕ_- degree of freedom) the differential short MI could no longer hold lock.

Models that were developed in parallel with the benchtop experiments showed that useful tunings for

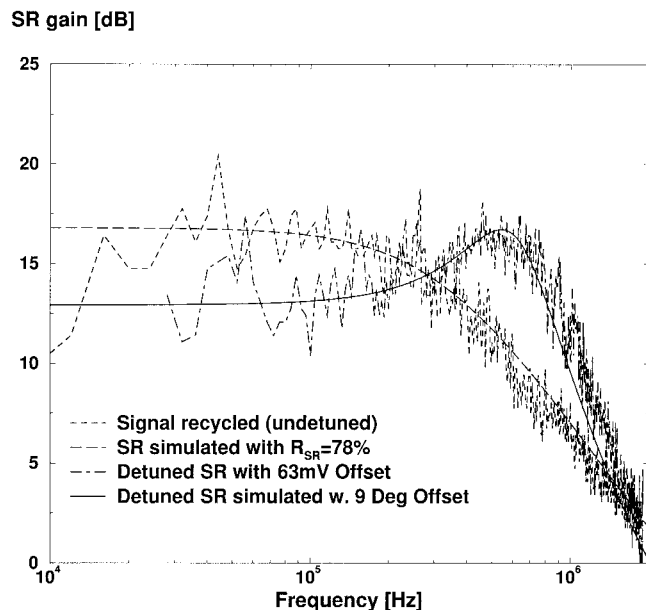


Fig. 9. SR gain for a resonant and a detuned SR cavity, measured and simulated. We achieved the detuning by adding a dc offset to the SR error signal.

a real gravitational-wave detector are between 83° and 89° away from dual recycling.⁵ In the present experiment, we could not reach this detuning range. However, the principals of our length-sensing scheme do not require that the starting configuration be dual recycling. A change in the length of the SR cavity such that the 31.8-MHz sidebands are resonant at the resonant extraction tuning would allow us to lock the interferometer at that point. Starting from there, a 10° detuning would cover the interesting tuning range. However, the double-demodulation technique⁸ has many advantages and is the technique that is proposed for the Advanced LIGO.

5. Discussion and Summary

In summary, we have described and demonstrated a length-sensing and control scheme for a dual-recycled cavity-enhanced Michelson interferometer, the optical configuration of the Advanced LIGO. We have thoroughly characterized the benchtop experiment and measured the frequency response for various tunings. With our tuning technique, we were limited to a detuning of 10° from the dual-recycling point.

Nevertheless, the experimental results show that it is possible to lock the dual-recycled cavity-enhanced Michelson interferometer with two pairs of phase modulation sidebands. The modulation frequencies can be chosen in such a way that both pairs can pass a single-mode cleaner. This modulation scheme is now proposed for the Advanced LIGO. However, the final sensing and control scheme merges all three schemes presented in this issue. A full discussion of the baseline design and how the results of the three groups influenced the baseline design is provided in Strain *et al.*⁶

References and Notes

1. A. Abramovici, W. Althouse, R. Drever, Y. Gursel, S. Kawamura, F. Raab, D. Shoemaker, L. Sievers, R. Spero, K. Thorne, R. Vogt, R. Weiss, S. Whitcomb, and M. Zucker, "LIGO: the Laser Interferometer Gravitational-Wave Observatory," *Science* **256**, 325–333 (1992).
2. K. Danzmann, H. Lück, A. Rüdiger, R. Schilling, M. Schrempel, W. Winkler, J. Hough, G. P. Newton, N. A. Robertson, H. Ward, A. M. Campbell, J. E. Logan, D. I. Robertson, K. A. Strain, J. R. J. Bennett, V. Kose, M. Kühne, B. F. Schutz, D. Nicholson, J. Shuttleworth, H. Welling, P. Aufmuth, R. Rinkler, A. Tünnermann, and B. Willke, "GEO 600—a 600-m Laser interferometric gravitational wave antenna," in *First Edoardo Amaldi Conference on Gravitational Wave Experiments*, E. Coccia, G. Pizella, and F. Ronga, eds. (World Scientific, Singapore, 1995), pp. 100–111.
3. K. Tsubono, "300-m laser interferometer gravitational wave detector (TAMA300) in Japan," in *First Edoardo Amaldi Conference on Gravitational Wave Experiments*, E. Coccia, G. Pizella, and F. Ronga, eds. (World Scientific, Singapore, 1995), pp. 112–114.
4. C. Bradaschia, R. Del Fabbro, A. Di Virgilio, A. Giazotto, H. Kautzky, V. Montelatici, D. Passuello, A. Brillet, O. Cregut, P. Hello, C. N. Man, P. T. Manh, A. Marraud, D. Shoemaker, J. Y. Vinet, F. Barone, L. Di Fiore, L. Milano, G. Russo, J. M. Aguirregabiria, H. Bel, J. P. Duruisseau, G. Le Denmat, Ph. Tourrenc, M. Capozzi, M. Longo, M. Lops, I. Pinto, G. Rotoli, T.

- Damour, S. Bonazzola, J. A. Marck, Y. Gourgoulon, L. E. Holloway, F. Fuligni, V. Iafolla, and G. Natale, "The VIRGO project: a wide band antenna for gravitational wave detection," *Nucl. Instrum. Methods Phys. Res. A* **289**, 518–525 (1990).
5. LIGO Science Collaboration, "Advanced LIGO systems design," P. Fritschel, ed., LIGO Tech. Note T010075; available from the LIGO Document Control Center at <http://antares.ligo.caltech.edu/dcc/default.htf> (2001); also see documents in www.ligo.caltech.edu/ligo2.
 6. K. A. Strain, G. Müller, T. Delker, D. H. Reitze, D. B. Tanner, J. E. Mason, P. A. Willems, D. A. Shaddock, M. B. Gray, C. Mow-Lowry, and D. E. McClelland, "Sensing and control in dual-recycling laser interferometer gravitational-wave detectors," *Appl. Opt.* **42**, 1244–1256 (2003).
 7. J. E. Mason and P. A. Willems, "Signal extraction and optical design for an advanced gravitational-wave interferometer," *Appl. Opt.* **42**, 1269–1282 (2003).
 8. D. A. Shaddock, M. B. Gray, C. Mow-Lowry, and D. E. McClelland, "Power-recycled Michelson interferometer with resonant sideband extraction," *Appl. Opt.* **42**, 1283–1295 (2003).
 9. S. Yoshida, G. Mueller, T. Delker, Q. Shu, D. Reitze, D. B. Tanner, J. Camp, J. Heefner, B. Kells, N. Mavalvala, D. Ouimette, H. Rong, R. Adhikari, P. Fritschel, M. Zucker, and D. Sigg, "Recent development in the LIGO input optics," in *Proceedings of the Second Tama International Workshop on Gravitational Wave Detection* (Universal Academy, Tokyo, Japan, 1999), pp. 51–59.
 10. D. Jackrel, "High-power high-efficiency photodiode for advanced LIGO," LIGO Document G010359-00; available from the LIGO Document Control Center at <http://antares.ligo.caltech.edu/dcc/default.htf>.
 11. The optimization of the parameters, the amplitudes of the different frequency components in the various ports of the interferometer, the locking matrix, and the sensitivities were modeled with a software package called Finesse, written by Andreas Freise. Information about Finesse can be found on the Software Tools for Advanced Interferometer Configurations webpage at www.phys.ufl.edu/LIGO/LIGO/STAIC.html or at www.mpg.de/~adf.